SMASIS2022-89315

IMPLEMENTATION OF AN ORIGAMI DYNAMICS MODEL BASED ON THE ABSOLUTE NODAL COORDINATE FORMULATION (ANCF)

Jiayue Tao,[*] **and Suyi Li**
Department of Mechanical Engineering
Clemson University, Clemson, SC 29634

ABSTRACT

Origami — the ancient art of paper folding — has been widely adopted as a design and fabrication framework for many engineering applications, including multi-functional structures, deployable spacecraft, and architected materials. These applications typically involve complex and dynamic deformations in the origami facets, necessitating high-fidelity models to better simulate folding-induced mechanics and dynamics. This paper presents the formulation and validation of such a new model based on the Absolute Nodal Coordinate Formulation (ANCF), which exploits the tessellated nature of origami and describes it as an assembly of flexible panels rotating around springy creases. To estimate the crease folding, we mathematically formulate a "torsional spring connector" in the framework of ANCF and apply it to the crease nodes, where the facets meshed by ANCF plate elements are interconnected. We simulate the dynamic folding of a Miura-ori unit cell and compare the results with commercial finite element software (ABAQUS) to validate the modeling accuracy. The ANCF model can converge using significantly fewer elements than ABAQUS without sacrificing accuracy. Therefore, this high-fidelity model can help deepen our knowledge of folding-induced mechanics and dynamics, broadening the appeals of origami in science and engineering.

Keywords: Origami Dynamics, Torsional Spring Connector, Absolute Nodal Coordinate Formulation (ANCF)

---

[*]Address all correspondence to this author: jiayuet@g.clemson.edu

1 INTRODUCTION

Origami is an ancient recreational art of paper folding. Over the past decades, it has evolved into a framework for designing and fabricating various engineering systems, such as multistable structures [1, 2], deployable spacecraft [3–5], self-folding robots [6–10], and DNA machines [11]. In these applications, origami is a shape transformation mechanism for developing programmed 3D shapes from flat sheets, and its folding and deformation play a crucial role in the targeted functions. The increasingly diverse applications of origami require us to better understand the mechanics and dynamics induced by folding, especially in the case of large facet deformation and rotation. To this end, many analytical and numerical models are available for this purpose with different degrees of capabilities.

According to their folding kinematics and deformation characteristics, there are two categories of origami: one is rigid-foldable, and the other is non-rigid foldable. Rigid-foldable origami can fold even if its facets are rigid, so its deformation can be characterized as facets revolving around hinge-like creases just like a linkage mechanism [3]. Correspondingly, the *rigid facet approach* can model these rigid-foldable origamis without unnecessary complexities. In this approach, facet deformations are neglected, and the creases are modeled as hinges with assigned torsional stiffness. In this way, one can quickly analyze the kinematics and mechanics of rigid-foldable origami, like the classical Miura-ori [12, 13]. Moreover, this approach can directly demonstrate the correlations between folding kinematics and some mechanical properties (e.g., negative Poisson's ratio [14, 15]). However, this approach is no longer applicable when the facet deformation is not negligible.

Non-rigid foldable origami exhibits facet deformation during folding, including stretching, shearing, bending, twisting, and even localized buckling [16]. The deformation patterns of non-rigid foldable origamis can be pretty complex, but they can also lead to unique mechanical properties that rigid-foldable origami can not provide. For example, Kresling origami can provide multi-stability due to facet bending [17]. The out-of-plane bending of Miura-ori, which also induces facet deformations, leads to an unorthodox combination of positive and negative Poisson's ratio [14]. Currently, two modeling approaches are available for the non-rigid foldable origami. The first one is the widely used *bar-hinge approach* [18, 19], which discretizes the continuous origami sheets into pin-jointed truss-frame systems. It represents creases with stretchable bar elements and assigns rotational spring coefficients to creases folding and facet bending. By using this approach, one can simulate simple facet bending and stretching. The bar-hinge approach is more advantageous when the macroscopic response is of interest because it can provide qualitatively accurate predictions on folding kinematics and mechanical properties on a global scale [20, 21]. However, the disadvantage of this approach is that it can not guarantee accuracy when complex and localized facet and crease deformation exists. Moreover, due to its underpinning simplification, the bar-hinge approach can not provide detailed results such as stress distribution along the creases or across facets [16].

The third *finite element approach* does not impose any explicit simplifications on the facet and crease deformation [3, 13, 20, 22–24], so it can perform eigenanalysis to analyze the deformation modes of origami accurately. It is often used to validate the results from the other approaches. Moreover, localized facet and crease deformations, such as the buckling and crushing due to impacts, can be examined in detail [25, 26]. However, local instabilities may negatively influence the global convergence of finite element simulations, even leading to element failure, especially when significant rotation exists.

Therefore, there is still a critical demand for a high-fidelity mechanics and dynamics model for non-rigid foldable origami. On the one hand, origami folding in practical application always involves complicated behaviors beyond simple rigid folding due to the inevitable facet compliance and fabrication imperfection. This is more evident when facet deformation is even desired, like in the Sunshield [27] and flasher origami deployment [4]. On the other hand, non-rigid origami can provide more structural and material functionalities by relaxing the facet compliance due to their richer deformation modes.

This study aims to develop and validate a new origami model based on the Absolute Nodal Coordinate Formulation (ANCF). With this model, dynamics of non-rigid origami can be simulated with quantitative accuracy, even when significant facet and crease deformation exist during folding. Another advantage of the ANCF model is that it can provide an excellent approximation of flexible structures' behavior while requiring fewer ele-

ments than the commercial finite element software (e.g., ANSYS) for convergence [28, 29]. A previous study by the authors developed a preliminary formulation for the ANCF model for origami [30], so this study aims to complete and validate this new model. In what follows, Section 2 briefly reviews the fundamentals of ANCF. Section 3 details how the ANCF can be adapted to origami, emphasizing crease modeling. Section 4 presents the model validation based on a simple Miura-ori unit cell. Section 5 concludes this paper with a summary and discussion.

2 ABSOLUTE NODAL COORDINATE FORMULATION
In this section, we briefly review the fundamental kinematics and dynamics modeling principles underpinning the Absolute Nodal Coordinate Formulation.

2.1 Kinematics of ANCF Plate Elements
The ANCF uses *position* and *position gradients* as the element nodal coordinates, rather than displacement and infinitesimal rotations in the traditional finite element setup. In this study, we apply fully parameterized ANCF thick plate elements for Miura-ori (Figure 1). The global position vector $\mathbf{r}$ of an arbitrary point P located on the plate element is:

$$\mathbf{r}(\mathbf{x},t) = \mathbf{S}(\mathbf{x})\mathbf{e}(t), \tag{1}$$

where $\mathbf{S}$ is the element shape function detailed in the Appendix. $\mathbf{x} = \begin{bmatrix} x\ y\ z \end{bmatrix}^{\mathsf{T}}$ is the spatial coordinates of the point defined in the element coordinate system, and $\mathbf{e}$ is the vector of the element nodal coordinates. Because $\mathbf{r}$ are directly defined in the global coordinate system $\mathbf{X} = \begin{bmatrix} X\ Y\ Z \end{bmatrix}^{\mathsf{T}}$, there is no need to transform
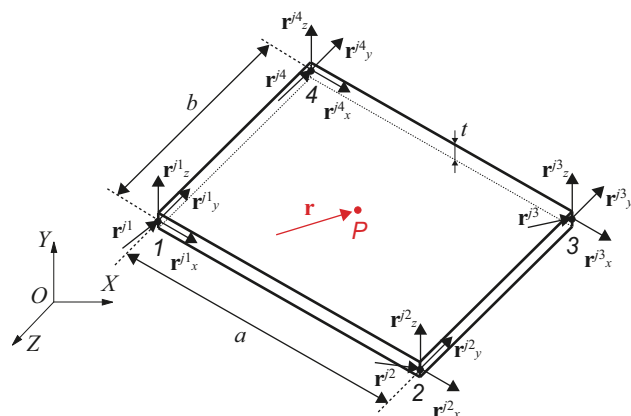

FIGURE 1: A fully parameterized ANCF plate element. It has four nodes, and each node has one position vector and three position gradient vectors.

the coordinate system when assembling plate elements. The vector of element nodal coordinates at node k of the element $\#j$ is defined in the following form:

$$\mathbf{e}^{jk} = \left[(\mathbf{r}^{jk})^\top \ (\mathbf{r}_x^{jk})^\top \ (\mathbf{r}_y^{jk})^\top \ (\mathbf{r}_z^{jk})^\top \right]^\top. \tag{2}$$

Here $\mathbf{r}^{jk}$ represents the vector of absolute position vector of node k ($k = 1, 2, 3, 4$) on element j, while the position vector gradients are defined by $\mathbf{r}_x^{jk} = \partial \mathbf{r}^{jk} / \partial x$, $\mathbf{r}_y^{jk} = \partial \mathbf{r}^{jk} / \partial y$ and $\mathbf{r}_z^{jk} = \partial \mathbf{r}^{jk} / \partial z$. These position vector gradient vectors can be used to describe the shape of the element during deformation [31]. Each node consists of twelve nodal coordinates, resulting in 48 degrees of freedom for each element, as shown in Figure 1.

2.2 Element Equation of Motion
The ANCF element equations of motion can be written in a matrix form as [32]

$$\mathbf{M}\ddot{\mathbf{e}} + \mathbf{Q}_s = \mathbf{Q}_e. \tag{3}$$

In this equation, $\mathbf{M}$ is the element mass matrix that can be obtained from the kinetic energy

$$T = \frac{1}{2} \int_V \rho \dot{\mathbf{r}}^\top \dot{\mathbf{r}} dV, \tag{4}$$

where ρ is the element mass density, V is the element volume, and $\dot{\mathbf{r}}$ is the absolute velocity vector. Differentiating Equation (1) with respect to time, one can obtain $\dot{\mathbf{r}} = \mathbf{S}\dot{\mathbf{e}}$, which is substituted into Equation (4) yielding $T = \frac{1}{2}\dot{\mathbf{e}}^\top \mathbf{M}\dot{\mathbf{e}}$. The element mass matrix $\mathbf{M}$ is

$$\mathbf{M} = \int_V \rho \mathbf{S}^\top \mathbf{S} dV. \tag{5}$$

The traditional plate and shell elements in large deformation and rotation analysis have nonlinear mass matrices because they include information about the nodal rotations. However, the mass matrix in the ANCF element is constant since it only depends on the inertia properties and element dimensions.

The generalized elastic force vector $\mathbf{Q}_s$ can be formulated using the continuum mechanics approach, which has the advantage of being general without any approximations [33]. The Green Lagrange strain tensor can be written in terms of the matrix of position vector gradient $\mathbf{J}$ in the following form

$$\boldsymbol{\varepsilon} = \frac{1}{2}(\mathbf{J}^\top \mathbf{J} - \mathbf{I}). \tag{6}$$

where $\mathbf{I}$ is 3×3 identity matrix, and $\mathbf{J}$ is obtained as

$$\mathbf{J} = \frac{\partial \mathbf{r}}{\partial \mathbf{X}} = \begin{bmatrix} \frac{\partial \mathbf{S}_1}{\partial X}\mathbf{e} & \frac{\partial \mathbf{S}_1}{\partial Y}\mathbf{e} & \frac{\partial \mathbf{S}_1}{\partial Z}\mathbf{e} \\ \frac{\partial \mathbf{S}_2}{\partial X}\mathbf{e} & \frac{\partial \mathbf{S}_2}{\partial Y}\mathbf{e} & \frac{\partial \mathbf{S}_2}{\partial Z}\mathbf{e} \\ \frac{\partial \mathbf{S}_3}{\partial X}\mathbf{e} & \frac{\partial \mathbf{S}_3}{\partial Y}\mathbf{e} & \frac{\partial \mathbf{S}_3}{\partial Z}\mathbf{e} \end{bmatrix}. \tag{7}$$

Here $\mathbf{S}_i$ is the ith row of the shape function matrix as provided in Appendix, and X, Y, Z are the global coordinates. Therefore, the strain energy using the general continuum mechanics approach is formulated in terms of the Green-Lagrange strain tensor $\boldsymbol{\varepsilon}$ and the elastic coefficients matrix $\mathbf{E}$ so that

$$U = \int_V \boldsymbol{\varepsilon}^\top \mathbf{E}\boldsymbol{\varepsilon} dV. \tag{8}$$

By differentiating the strain energy once with respect to the nodal coordinates, we can obtain the generalized elastic force vector $\mathbf{Q}_s$ as

$$\mathbf{Q}_s = \int_V \left(\frac{\partial \varepsilon_v}{\partial \mathbf{e}} \right)^\top \mathbf{E}\varepsilon_v dV, \tag{9}$$

where ε_v is the vector form of the Green-Lagrange strain tensor. The resulting vector of generalized elastic forces is highly nonlinear due to the general continuum mechanics approach without linearization.

The vector $\mathbf{Q}_e$ is generalized external force vector due to inter-element constraints, detailed in the following Section 3.

3 ORIGAMI DYNAMIC MODEL BASED ON ANCF
As mentioned earlier, origami folding involves facets revolving around the creases [3]. The bar-hinge model treats the creases as hinges with prescribed rotational springs between two neighboring facets. This method proved successful for qualitatively predicting the global folding behaviors and mechanical properties [2, 3]. Inspired by this, we propose to exploit the tessellated nature of origami and model it by ANCF plate elements rotating around the creases. For example, the Miura-ori can be meshed by ANCF plate elements, and they are linked by the "torsional spring connectors" at their overlapping nodes along the creases (Figure. 2). For simplicity, each Miura-ori facet in this figure is meshed by one ANCF plate element (i.e., the facet (I) is one plate element with nodes 1-2-4-3, and facet (II) has nodes 1-2-6-5), and they are interconnected by the folding crease 1-2. One can use a finer mesh for better accuracy, but the basic principle is the same. We further assume the facet deforms from an initially flat parallelogram shape to a curved surface at the current configuration (Figure 2).
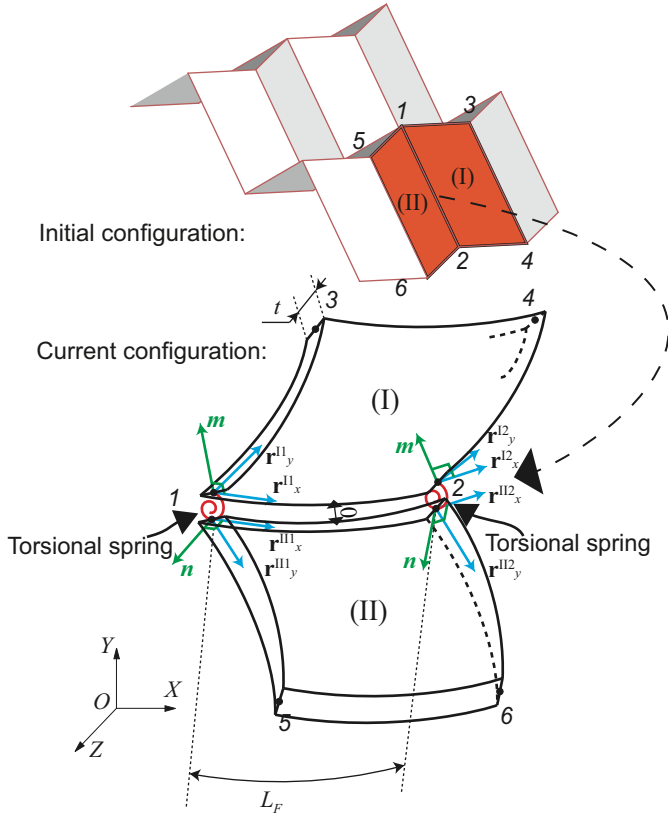
FIGURE 2: Kinematic modeling of origami crease in the ANCF framework. For simplicity, we assume each facet is an ANCF plate element, whereas the crease is modeled by rotational springs at nodes 1 and 2. The magnitude of crease folding (or relative facet rotation) is measured by folding angle θ defined based on the position gradients at the crease nodes, respectively.

To model the crease folding, we assign revolute joints at the interconnected crease nodes 1 and 2, which means that the two plates share the same position at these nodes, and the position gradient along the common crease is the same. Such revolute joint kinematics can be expressed as the continuity conditions at nodes 1 and 2:

$$\mathbf{r}^{I1} = \mathbf{r}^{I1}, \ \mathbf{r}_x^{I1} = \mathbf{r}_x^{III}, \ \text{at node 1}, \\ \mathbf{r}^{I2} = \mathbf{r}^{II2}, \ \mathbf{r}_x^{I2} = \mathbf{r}_x^{II2}, \ \text{at node 2}. \tag{10}$$

With the revolute joint constraints, there is only one relative rotational degree of freedom at nodes 1 and 2. Moreover, one can see that the corresponding rotational axis is tangent to the crease line at the nodes, which is the common position gradient vector along the local x-axis. Then we can apply the torsional spring connectors developed in the ANCF framework at these crease

nodes to simulate folding (the red spirals at nodes 1 and 2 in Figure 2). To this end, we first need to develop the mathematical formulation of the connector's constraint equations in the ANCF framework.

An important variable to be determined is the folding angle between adjacent facets at the crease nodes. Calculating this angle is not trivial because the nodal coordinates in ANCF are the position gradients rather than rotation angle. To this end, we first introduce the local normal vectors $\mathbf{m}$ and $\mathbf{n}$ at node k in facets I and II, respectively ($k = 1, 2$ in the example in Figure 2):

$$\mathbf{m} = (\mathbf{r}_x^{Ik} \times \mathbf{r}_y^{Ik}) \times \mathbf{r}_x^{Ik}, \\ \mathbf{n} = (\mathbf{r}_x^{IIk} \times \mathbf{r}_y^{IIk}) \times \mathbf{r}_x^{Ik}. \tag{11}$$

Here, the operator '$\times$' between two vectors represents the cross product. This formulation guarantees that the directional vector $\mathbf{m}$ and $\mathbf{n}$ are always perpendicular to the crease revolute joint's rotational axis at node k. Therefore, one can calculate the folding angle, at the current configuration, between two facets at node k based on trigonometry functions in that:

$$\theta_k = \arccos\left(\frac{\mathbf{m} \cdot \mathbf{n}}{\|\mathbf{m}\| \cdot \|\mathbf{n}\|}\right) \ \text{mod} \ 2\pi, \tag{12}$$

where the symbol 'mod' means modulo operation. Once the folding angle is determined, one can then calculate the resistant moment by the added torsional spring connector as

$$M_k = k_f(\theta_k - \theta_{k,0}) + c_f \dot{\theta}_k + M_a, \tag{13}$$

where k_f is the localized torsional spring coefficient at node k, c_f is the damping coefficient, and M_a is the external moment applied to the torsional spring (if it exists). $\theta_{k,0}$ is the stress-free folding angle corresponding to the origami's resting configuration.

In the simplified example in Figure 2, the origami crease between facets (I) and (II) is represented by two rotational springs at nodes 1 and 2. Therefore, one can evenly distribute the total crease folding stiffness k_l to each rotational spring so that $k_f = 0.5k_l$, where k_l can be experimentally measured.

The virtual work by the added torsional spring connector is

$$\delta W_k = -M_k \delta \theta_k. \tag{14}$$

Based on the continuum mechanics approach [34], one can derive the virtual angular displacement $\delta\theta_k = \mathbf{h}^\mathsf{T}(\mathbf{G}^I\delta\mathbf{e}^I - \mathbf{G}^{II}\delta\mathbf{e}^{II})$, where $\mathbf{h}$ represents the vector of revolute joint's rotational axis, $\mathbf{G}$ is linear operator to obtain ANCF generalized moment associated with the nodal coordinates in facets I and II.

TABLE 1: Design parameters of the Miura-ori unit cell

Geometry	Value	Material	Value
a	20 mm	ρ	1384 kg/m^3
b	20 mm	E	57.9 MPa
t	1.24 mm	v	0.3894
γ	40°	k_l	2 N.mm/rad

Based on these formulations, the virtual work can be re-written as

$$\delta W_k = -M_k \mathbf{h}^\mathsf{T} \left(\mathbf{G}^\mathrm{I} \delta \mathbf{e}^\mathrm{I} - \mathbf{G}^\mathrm{II} \delta \mathbf{e}^\mathrm{II} \right) = \mathbf{Q}_k^{\mathrm{I}\mathsf{T}} \delta \mathbf{e}^\mathrm{I} + \mathbf{Q}_k^{\mathrm{II}\mathsf{T}} \delta \mathbf{e}^\mathrm{II}. \quad (15)$$

Therefore, the torsional spring connector is equivalent to two equal but opposite generalized external moment acting on the nodes along the crease, that is, $\mathbf{Q}_k^{\mathrm{I}\mathsf{T}} = -M_k \mathbf{h}^\mathsf{T} \mathbf{G}^\mathrm{I}$ and $\mathbf{Q}_k^{\mathrm{II}\mathsf{T}} = M_k \mathbf{h}^\mathsf{T} \mathbf{G}^\mathrm{II}$ in Equation (15). $\mathbf{Q}_k^{\mathrm{I}\mathsf{T}}$ and $\mathbf{Q}_k^{\mathrm{II}\mathsf{T}}$ can be inserted into Equation (3) by standard finite element procedures.

It is worth highlighting that based on the proposed ANCF approach, the definition of folding angle θ in Equation (12) also applies to origami with a curved crease pattern and initially curved facets. Such versatility presents a clear advantage compared to the currently popular bar-hinge model, which assumes that the facet defined by three bar elements must remain planar. Furthermore, the model allows us to simulate complex origami dynamics using a relatively small number of elements, as we explain in detail in the following section on modal validation.

4 VALIDATION OF ANCF ORIGAMI MODEL

In this section, we aim to verify the accuracy of the proposed ANCF model in origami application by simulating the dynamic folding of a single Miura-ori unit cell. The Miura-ori's geometry and material parameters are summarized in Figure 3 and Table 1. a, b are the crease lengths, γ is the sector angle between the two creases, and t is the material thickness. The constitutive material properties (density ρ, Young's modulus E, Poisson's ratio μ, and crease folding stiffness k_l) are measured from samples made by Nylon material. The Miura-ori cell is initially flat, so the resting folding angle $\theta_{k,0} = 0$ for all creases.

Figure 3 details the Miura-ori simulation setup. In this case, the unit cell is subjected to an impact force along the global z-axis at the *center node A* with magnitude $F_z = 0.1N$, generating a transient dynamic response. The cell is meshed by the ANCF plate element, and the torsional spring connectors are applied to all nodes along the four creases. As mentioned in Section 3, we evenly distribute the total torsional stiffness of a crease to the corresponding nodes. Therefore, each torsional spring connector
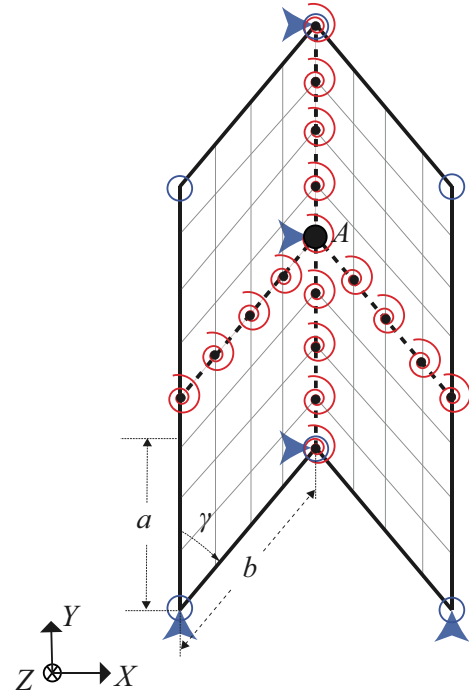

FIGURE 3: Dynamic simulation setup of the Miura-ori unit cell's folding under z-axial concentrated force at the center node A. The blue arrows represent the displacement constraints in either the x or y axis, whereas the blue hollow circle represents the z-axis constraint. We add the proposed torsional spring connectors (the red spirals) at N folding crease nodes (the black solid circle). Here, there are 4×4 ANCF plate elements in each Miura-ori facet, giving five nodes on each crease ($N = 5$).

has $k_f = \frac{1}{N} k_l$, where k_l is the total torsional stiffness of a crease, N is the number of nodes along this crease.

We use the Sigma/Sams software package to perform the dynamic solution (developed by Dr. Ahmed A. Shabana's research group, Dynamic Simulation Laboratory, at the University of Illinois, Chicago). Explicit Adams Method (EAM) is used to solve the dynamic equations of motion in Equation (3) [35]. Figure 4(a) summarizes the time response of the center node A's vertical displacement based on the ANCF model (solid lines), and Figure 4(b) highlights some simulated Miura-ori deformation. We also conducted finite element simulations using the commercial software package ABAQUS for validation. In ABAQUS, the unit cell is meshed by the 3D continuum shell elements (SC8R, 8-node quadrilateral elements with reduced integration). Hinge connectors are assigned along the crease with prescribed torsional stiffness k_l. The solver is dynamic explicit, which considers the geometrical nonlinearity effects.

The results show that 144 ANCF plate elements are sufficient to achieve convergence, whereas 2312 FEA elements are required in ABAQUS. The relative error of $z-$axis displacement

(a)

(b)

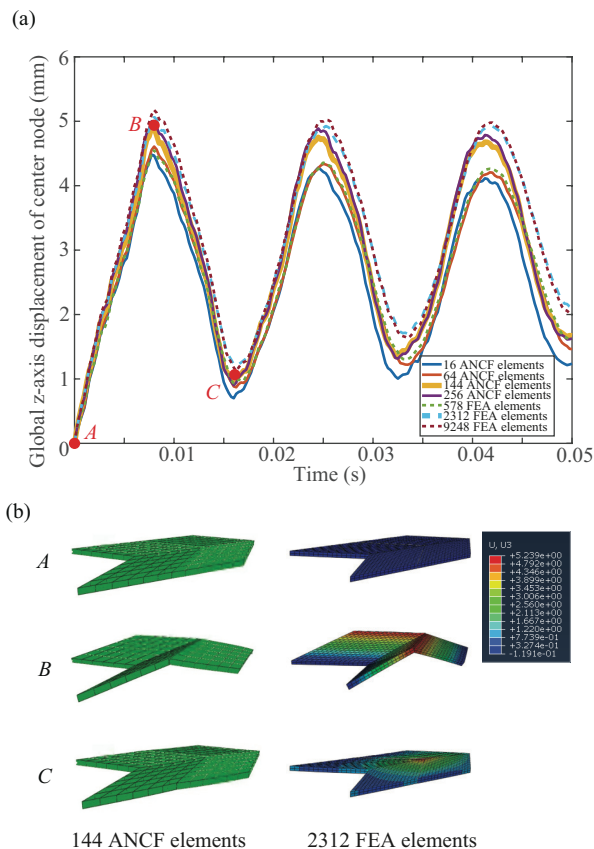

144 ANCF elements   2312 FEA elements

FIGURE 4: Summary of the simulation results. a) Time response of the center node A's out-of-plane displacement, based on ANCF and commercial finite element approach with different mesh sizes. b) The simulated dynamic Miura-ori deformations at three different time instants (aka., A, B, C on the response curves). Colors in the commercial FEA results represent the magnitude of global displacement in the z-axis.

at center node between ANCF model and FEA model is 3.92% at point *B* and 8.33% at point *C*, respectively. The discrepancy might be due to the different numerical solvers used by the two methods, which requires further studies in the future. But more importantly, by using the position gradient vectors instead of rotations, the ANCF model has no assumptions about the magnitude of rotations within the elements. This allows the Miura-ori to be represented by fewer elements. The results in Figure 4 validate that the ANCF model requires significantly fewer elements to obtain convergence by comparing to the traditional finite element methods.

5 CONCLUSION

Traditionally, origami folding has been investigated as a geometrical and kinematic problem. However, the nonlinear mechanics

and dynamics of origami have received more interest recently because, in practical implementation, complex facet deformations beyond simple folding along the creases are inevitable or even desired. To facilitate the in-depth investigation of the dynamics induced by folding, we formulate and validate a new origami model based on the Absolute Nodal Coordinate Formulation (ANCF). This ANCF model exploits the tessellated nature of origami and meshes it with ANCF plate elements linked by torsional spring connectors along creases. The mathematical formulation of the torsional spring connectors is constructed and implemented into the ANCF framework. Finally, the governing dynamic equations of motion for origami folding are obtained. To validate the accuracy of the proposed ANCF model, we use it to simulate the dynamic folding of a Miura-ori unit cell under point force and compare the results to the commercial finite element software package (ABAQUS). The results show that the ANCF model can converge with much fewer elements than ABAQUS without sacrificing accuracy.

The proposed ANCF model provides a robust and high-fidelity simulation tool for the kinematics analysis of origami folding globally. It can also reveal the constituent panels and creases' underlying mechanics and dynamics responses. Moreover, it has the potential to accurately simulate origami's deformation even when large facet deformation and rotation exist. This is because the ANCF element can analyze large deformation without causing excessive rotation problems as it has in the traditional finite element approach.

ACKNOWLEDGMENT

REFERENCES

[1] Fang, H., Wang, K., and Li, S., 2017. "Asymmetric energy barrier and mechanical diode effect from folding multistable stacked-origami". *Extreme Mechanics Letters*, *17*, nov, pp. 7–15.

[2] Tao, J., and Li, S., 2021. "A study of the multi-stability in a non-rigid stacked miura-origami cellular mechanism". *Proceedings of the ASME Design Engineering Technical Conference*, *8B-2021*, pp. 1–9.

[3] Li, S., Fang, H., Sadeghi, S., Bhovad, P., and Wang, K. W., 2019. "Architected Origami Materials: How Folding Creates Sophisticated Mechanical Properties". *Advanced Materials*, *31*(5), pp. 1–18.

[4] Zirbel, S. A., Lang, R. J., Thomson, M. W., Sigel, D. A., Walkemeyer, P. E., Trease, B. P., Magleby, S. P., and How-

Copyright © 2022 by ASME

ell, L. L., 2013. "Accommodating thickness in origami-based deployable arrays1". *Journal of Mechanical Design, Transactions of the ASME, 135*(11), pp. 1–11.

[5] Schenk, M., Viquerat, A. D., Seffen, K. A., and Guest, S. D., 2014. "Review of Inflatable Booms for Deployable Space Structures: Packing and Rigidization". *Journal of Spacecraft and Rockets, 51*(3), may, pp. 762–778.

[6] Felton, S., Tolley, M., Demaine, E., Rus, D., and Wood, R., 2014. "A method for building self-folding machines". *Science, 345*(6197), pp. 644–646.

[7] Pagano, A., Yan, T., Chien, B., Wissa, A., and Tawfick, S., 2017. "A crawling robot driven by multi-stable origami". *Smart Materials and Structures, 26*(9).

[8] Firouzeh, A., and Paik, J., 2015. "Robogami: A Fully Integrated Low-Profile Robotic Origami". *Journal of Mechanisms and Robotics, 7*(2), pp. 1–8.

[9] Miyashita, S., Guitron, S., Li, S., and Rus, D., 2017. "Robotic metamorphosis by origami exoskeletons". *Science Robotics, 2*(10).

[10] Fang, H., Zhang, Y., and Wang, K. W., 2017. "Origami-based earthworm-like locomotion robots". *Bioinspiration and Biomimetics, 12*(6).

[11] Wang, P., Meyer, T. A., Pan, V., Dutta, P. K., and Ke, Y., 2017. "The Beauty and Utility of DNA Origami". *Chem, 2*(3), pp. 359–382.

[12] Gattas, J. M., Wu, W., and You, Z., 2013. "Miura-base rigid origami: Parameterizations of first-level derivative and piecewise geometries". *Journal of Mechanical Design, Transactions of the ASME, 135*(11), pp. 1–11.

[13] Zhou, X., Zang, S., and You, Z., 2016. "Origami mechanical metamaterials based on the Miura-derivative fold patterns". *Proceedings of the Royal Society A: Mathematical, Physical and Engineering Sciences, 472*(2191).

[14] Schenk, M., and Guest, S. D., 2013. "Geometry of Miura-folded metamaterials". *Proceedings of the National Academy of Sciences of the United States of America, 110*(9), feb, pp. 3276–3281.

[15] Wei, Z. Y., Guo, Z. V., Dudte, L., Liang, H. Y., and Mahadevan, L., 2013. "Geometric mechanics of periodic pleated origami". *Physical Review Letters, 110*(21), pp. 1–5.

[16] Liu, K., and Paulino, G. H., 2017. "Nonlinear mechanics of non-rigid origami: An efficient computational approach". *Proceedings of the Royal Society A: Mathematical, Physical and Engineering Sciences, 473*(2206).

[17] Bhovad, P., Kaufmann, J., and Li, S., 2019. "Peristaltic locomotion without digital controllers: Exploiting multistability in origami to coordinate robotic motion". *Extreme Mechanics Letters, 32*, p. 100552.

[18] Li, S., and Wang, K. W., 2015. "Fluidic origami: a plant-inspired adaptive structure with shape morphing and stiffness tuning". *Smart Materials and Structures, 24*(10), oct, p. 105031.

[19] Mark, S., 2011. "Folded Shell Structures, PhD Thesis". PhD thesis, University of Cambridge.

[20] Gillman, A., Fuchi, K., and Buskohl, P. R., 2018. "Truss-based nonlinear mechanical analysis for origami structures exhibiting bifurcation and limit point instabilities". *International Journal of Solids and Structures, 147*, pp. 80–93.

[21] Liu, K., and Paulino, G. H., 2016. "MERLIN: A MATLAB implementation to capture highly nonlinear behavior of non-rigid origami". *Proceedings of IASS Annual Symposia (International Association for Shell and Spatial Structures), 2016*(13), pp. 1–10.

[22] Filipov, E. T., Paulino, G. H., and Tachi, T., 2016. "Origami tubes with reconfigurable polygonal cross-sections". *Proceedings of the Royal Society A: Mathematical, Physical and Engineering Sciences, 472*(2185).

[23] Fischer, S., 2015. "Realistic FE simulation of foldcore sandwich structures". *International Journal of Mechanical and Materials Engineering, 10*(1), dec, p. 14.

[24] Lv, C., Krishnaraju, D., Konjevod, G., Yu, H., and Jiang, H., 2014. "Origami based mechanical metamaterials". *Scientific Reports, 4*.

[25] Gattas, J. M., and You, Z., 2014. "Quasi-static impact of indented foldcores". *International Journal of Impact Engineering, 73*, pp. 15–29.

[26] Gattas, J. M., and You, Z., 2015. "The behaviour of curved-crease foldcores under low-velocity impact loads". *International Journal of Solids and Structures, 53*, pp. 80–91.

[27] Kidambi, N., and Wang, K. W., 2020. "Dynamics of Kresling Origami Deployment". *arXiv*, pp. 1–32.

[28] Obrezkov, L. P., Matikainen, M. K., and Harish, A. B., 2020. "A finite element for soft tissue deformation based on the absolute nodal coordinate formulation". *Acta Mechanica, 231*(4), apr, pp. 1519–1538.

[29] Ma, L., Wei, C., Ma, C., and Zhao, Y., 2020. "Modeling and Verification of a RANCF Fluid Element Based on Cubic Rational Bezier Volume". *Journal of Computational and Nonlinear Dynamics, 15*(4), apr.

[30] Tao, J., and Li, S., 2019. "SMASIS2019- 5534". pp. 1–12.

[31] Shabana, A. A., and Eldeeb, A. E., 2021. "Motion and shape control of soft robots and materials". *Nonlinear Dynamics*.

[32] Mikkola, A. M., and Shabana, A. A., 2003. "A non-incremental finite element procedure for the analysis of large deformation of plates and shells in mechanical system applications". *Multibody System Dynamics, 9*(3), pp. 283–309.

[33] Shabana, A. A., 2018. *Computational Continuum Mechanics*. Wiley.

[34] Recuero, A. M., Aceituno, J. F., Escalona, J. L., and Shabana, A. A., 2016. "A nonlinear approach for modeling rail flexibility using the absolute nodal coordinate formulation". *Nonlinear Dynamics, 83*(1-2), jan, pp. 463–481.

[35] Hussein, B., Negrut, D., and Shabana, A. A., 2008. "Implicit and explicit integration in the solution of the absolute nodal coordinate differential/algebraic equations". *Nonlinear Dynamics,* **54**(4), pp. 283–296.

Appendix A: Shape Functions of ANCF Plate Element

The shape functions are obtained using fourth-order polynomials, and they are

$$\mathbf{S}(\mathbf{x}) = [s_1\mathbf{I}, \ s_2\mathbf{I}, \ s_3\mathbf{I}, \ s_4\mathbf{I}, \ s_5\mathbf{I}, \ s_6\mathbf{I}, \ s_7\mathbf{I}, \ s_8\mathbf{I}, \ s_9\mathbf{I}, \ s_{10}\mathbf{I}, \dots$$
$$s_{11}\mathbf{I}, \ s_{12}\mathbf{I}, \ s_{13}\mathbf{I}, \ s_{14}\mathbf{I}, \ s_{15}\mathbf{I}, \ s_{16}\mathbf{I}] \tag{16}$$

where $\mathbf{I}$ is 3×3 identity matrix. The elements of the shape function matrix of the full parameterized plate element are given by

$$
\begin{aligned}
s_1 &= (2\xi + 1)(\xi - 1)^2(2\eta + 1)(\eta - 1)^2, \\
s_2 &= a\xi(\xi - 1)^2(2\eta + 1)(\eta - 1)^2, \\
s_3 &= b\eta(\xi - 1)^2(2\xi + 1)(\eta - 1)^2, \\
s_4 &= t\xi(\xi - 1)(\eta - 1), \\
s_5 &= -\xi^2(2\xi - 3)(2\eta + 1)(\eta - 1)^2, \\
s_6 &= a\xi^2(\xi - 1)(2\eta + 1)(\eta - 1)^2, \\
s_7 &= -b\eta\xi^2(2\xi - 3)(\eta - 1)^2, \\
s_8 &= t\zeta\xi(\eta - 1), \\
s_9 &= \eta^2\xi^2(2\xi - 3)(2\eta - 3), \\
s_{10} &= a\eta^2\xi^2(xi - 1)(2\eta - 3), \\
s_{11} &= -b\eta^2\xi^2(\eta - 1)(2\xi - 3), \\
s_{12} &= t\xi\zeta\eta, \\
s_{13} &= -\eta^2(2\xi + 1)(\xi - 1)^2(2\eta - 3), \\
s_{14} &= -a\xi\eta^2(\xi - 1)^2(2\eta - 3), \\
s_{15} &= -b\eta^2(\xi - 1)^2(2\xi + 1)(\eta - 1), \\
s_{16} &= -t\eta\zeta(\xi - 1).
\end{aligned}
\tag{17}
$$

Here $\xi = x/a$, $\eta = y/b$ and $\zeta = z/t$ while a, b and t are the plate length in x, y and z directions respectively (Figure 1).